Light Curve Modeling and Secular Analyses of the Totally Eclipsing Overcontact Binary System, V625 Hydrae

Kevin B. Alton
UnderOak Observatory, 70 Summit Avenue, Cedar Knolls, NJ 07927; kbalton@optonline.net

Received January 1, 2021; revised February 5, 2021; accepted February 8, 2021

Abstract Precise time-series CCD-derived photometric data (BVI_c) were acquired from V625 Hya at Desert Blooms Observatory in 2020. An updated linear ephemeris was calculated from sixteen new times of minimum (ToM) produced from these measurements along with thirteen other values from four ground-based surveys and the literature. Secular analyses (observed minus predicted ToM vs. epoch) revealed changes in the orbital period of V625 Hya over the past two decades, suggesting an apparent increase in the orbital period based on a parabolic fit of the residuals. In addition, simultaneous modeling of these multi-bandpass light curve data was accomplished using the Wilson-Devinney code. Since a total eclipse is observed, a photometrically derived value for the mass ratio (q_{ptm}) with acceptable uncertainty could be determined which consequently provided estimates for some physical and geometric elements of V625 Hya.

1. Introduction

Sparsely sampled monochromatic photometric data from V625 Hya (= NSVS 12914400) were first captured during the ROTSE-I survey between 1999 and 2000 (Akerlof *et al.* 2000; Woźniak *et al.* 2004). Gettel *et al.* (2006) included V625 Hya in their catalog of bright contact binary stars from the ROTSE-I survey while Hoffman *et al.* (2009) classified this system as a W UMa-type variable. Other sources of photometric data from this eclipsing binary included the All-Sky Automated Survey (ASAS: Pojmański *et al.* 2005), the All-Sky Automated Survey for SuperNovae (ASAS-SN: Shappee *et al.* 2014; Jayasinghe *et al.* 2018), the Catalina Sky Survey (CSS: Drake *et al.* 2014) and a multi-bandpass photometric study of W Ursae Majoris binaries by Terrell *et al.* (2012). Herein, the first multi-bandpass (BVI_c) light curves (LCs) from V625 Hya modeled with the Wilson-Devinney code (WD; Wilson and Devinney 1971; Wilson 1979, 1990) are reported. This investigation also includes secular analyses of the observed-minus-predicted eclipse timing differences (ETD) over the past 21 years.

2. Observations and data reduction

Precise time-series photometric observations were acquired in 2020 at Desert Blooms Observatory (DBO, USA: 31.941 N, 110.257 W) using a QSI 683 wsg-8 CCD camera mounted at the Cassegrain focus of a 0.4-m Schmidt-Cassegrain telescope. This focal-reduced (f/7.2) instrument produces an image scale of 0.76 arcsec/pixel (bin = 2 × 2) and a field-of-view (FOV) of 15.9 × 21.1 arcmin. The CCD camera was equipped with photometric B, V, and I_c filters manufactured to match the Johnson-Cousins Bessell specification. Image (science, darks, and flats) acquisition software (TheSkyX Pro Edition 10.5.0; Software Bisque 2019) controlled the main and integrated guide cameras. Computer time was updated immediately prior to each session. Dark subtraction, flat correction, and registration of all images collected at DBO were performed with AIP4Win v2.4.0 (Berry and Burnell 2005). Instrumental readings from V625 Hya were reduced to catalog-based magnitudes using APASS DR9 values (Henden *et al.* 2009, 2010, 2011; Smith *et al.* 2011) built into MPO Canopus v 10.7.1.3 (Minor Planet Obs. 2011).

Magnitude values for V625 Hya were produced from an ensemble of four comparison stars, the average of which remained constant (± 0.015 mag) throughout every imaging session. The identity, J2000 coordinates, and color indices (B–V) for these stars are provided in Table 1. A CCD image annotated with the location of the target (T) and comparison stars (1–4) is shown in Figure 1. Only data acquired above 30° altitude (airmass < 2.0) were evaluated; considering the close proximity of all program stars, differential atmospheric extinction was ignored. All photometric data acquired from V625 Hya at DBO can be retrieved from the AAVSO International Database (Kafka 2021).

3. Results and discussion

Results and detailed discussion about the determination of linear and quadratic ephemerides are provided in this Section. Thereafter, the multi-source approach for estimating the effective temperature of V625 Hya and Roche-lobe modeling results with the WD code are examined. Finally, preliminary estimates for mass ($M_\odot$) and radius ($R_\odot$), along with corresponding calculations for luminosity ($L_\odot$), surface gravity (log (g)), semi-major axis ($R_\odot$), and bolometric magnitude (M_{bol}), are derived.

Table 1. Astrometric coordinates (J2000), V-magnitudes, and color indices (B–V) for V625 Hya (Figure 1), and the corresponding comparison stars used in this photometric study.

Star Identification	*R.A. (J2000)*[a] *h m s*	*Dec. (J2000)*[a] ° ′ ″	*V-mag.*[b]	*(B–V)*[b]
(1) GSC 4867–1095	08 43 01.4248	–03 38 20.446	12.721	0.684
(2) GSC 4867–0905	08 43 18.2833	–03 44 54.223	12.275	0.562
(3) GSC 4867–1061	08 43 44.5488	–03 40 26.159	12.578	0.327
(4) GSC 4867–0766	08 44 07.4620	–03 39 27.861	11.868	0.452
(T) V625 Hya	08 43 03.9741	–03 42 52.541	11.702	0.751

a. R.A. and Dec. from Gaia DR2 (Gaia Collab. et al. *2016, 2018).*
b. V-mag and (B–V) for comparison stars derived from APASS DR9 database described by Henden et al. *2009, 2010, 2011 and Smith* et al. *2011.*

3.1. Photometry and ephemerides

A total of 245 photometric values in B-, 253 in V-, and 247 in I_c-passbands were acquired from V625 Hya at DBO between 03 December and 21 December 2020. Photometric uncertainty, which typically remained within ±0.004, was calculated according to the so-called "CCD Equation" (Mortara and Fowler 1981; Howell 2006). ToM values and associated errors from data acquired at DBO were calculated according to Andrych and Andronov (2019) and Andrych *et al.* (2020) using the program MAVKA (https://uavso.org.ua/mavka/). Around Min II, simulation of extrema was automatically optimized by finding the most precise degree (α) and best fit algebraic polynomial expression (Figure 2, top panel). During Min I, a "wall-supported line" (WSL) algorithm (Andrych *et al.* 2017) provided the best fit as the eclipse passes through totality, resulting in a flattened bottom (Figure 2, bottom panel). ToM differences (ETD) vs. epoch were fit using scaled Levenberg-Marquardt algorithms (QtiPlot 0.9.9-rc9; IONDEV SRL 2021).

Sixteen new ToM values were derived from photometric data acquired at DBO. An additional eleven ToM values were extrapolated from the NSVS, CSS, ASAS, and ASAS-SN surveys, along with two other observations gathered from the literature (Table 2). A new linear ephemeris based on near-term (2014–2021) results was determined as follows:

$$\mathrm{Min\,I\,(HJD)} = 2459204.72825\,(9) + 0.3485618\,(1)\,\mathrm{E}. \quad (1)$$

The difference (ETD) between observed eclipse times (Figure 3) and those predicted by the linear ephemeris against epoch (cycle number) reveals what appears to be a quadratic relationship where:

$$\mathrm{ETD} = -6.698 \pm 49.457 \cdot 10^{-5} + 4.0261 \pm 1.7500 \cdot 10^{-7}\,\mathrm{E} \\ 7.600 \pm 0.8634 \cdot 10^{-11}\,\mathrm{E}^2. \quad (2)$$

Given that the coefficient of the quadratic term (Q) is positive, this result would suggest that the orbital period has been increasing at the rate ($dP/dt = 2Q/P$) of 0.0138 ± 0.0016 $s \cdot y^{-1}$. This rate is similar to many other overcontact systems reported in the literature (Latković *et al.* 2021). Period change over time that can be described by a parabolic expression is often attributed to mass transfer or by angular momentum loss (AML) due to magnetic stellar wind (Qian 2001, 2003; Li *et al.* 2019). Ideally when AML dominates, the net effect is a decreasing orbital period. If conservative mass transfer from the more massive to its less massive secondary star prevails, then the orbital period can also decrease. Separation increases when conservative mass transfer from the less massive to its more massive binary cohort takes place or spherically symmetric mass loss from either body (e.g. a wind but not magnetized) occurs. In mixed situations (e.g. mass transfer from less massive star, together with AML) the orbit evolution depends on which process dominates.

[1] http://www.aerith.net/astro/color_conversion.html
[2] http://brucegary.net/dummies/method0.html

Table 2. V625 Hya times of minimum (20 April 1999–21 December 2020), cycle number, and residuals (ETD) between observed and predicted times derived from the updated linear ephemeris (Equation 1).

HJD 2400000+	*HJD Error*	*Cycle No.*	*ETD*[a]	*Reference*
51288.7463	0.0010	–22710.5	0.0311	1
51513.9111	0.0010	–22064.5	0.0250	1
51536.7427	0.0010	–21999	0.0258	1
52635.7510	0.0010	–18846	0.0187	2
52790.5167	0.0010	–18402	0.0229	3
53357.7951	0.0010	–16774.5	0.0170	2
53772.7511	0.0010	–15584	0.0102	2
53852.5766	0.0010	–15355	0.0150	2
55571.8447	0.0002	–10422.5	0.0020	4
55929.8215	0.0010	–9395.5	0.0057	3
55931.9044	0.0003	–9389.5	–0.0027	5
56751.7245	0.0010	–7037.5	0.0000	6
57753.6654	0.0010	–4163	0.0000	6
59190.9605	0.0002	–39.5	0.0005	7
59190.9606	0.0002	–39.5	0.0005	7
59192.8765	0.0004	–34	–0.0006	7
59192.8773	0.0004	–34	0.0001	7
59198.9771	0.0002	–16.5	0.0001	7
59198.9771	0.0004	–16.5	0.0001	7
59198.9778	0.0002	–16.5	0.0008	7
59200.8939	0.0001	–11	–0.0002	7
59200.8939	0.0001	–11	–0.0001	7
59200.8940	0.0001	–11	–0.0001	7
59202.9852	0.0004	–5	–0.0003	7
59202.9852	0.0001	–5	–0.0002	7
59202.9853	0.0001	–5	–0.0001	7
59204.9020	0.0003	0.5	–0.0005	7
59204.9026	0.0004	0.5	0.0001	7
59204.9026	0.0002	0.5	0.0001	7

a. ETD = Observed – Predicted Eclipse Time Difference.
References: 1. NSVS (Akerlof et al. *2000); 2. ASAS (Pojmański* et al. *2005); 3. CSS (Drake* et al. *2014); 4. Diethelm 2011; 5. Diethelm 2012; 6. ASAS-SN (Jayasinghe* et al. *2018); 7. This study.*

3.2. Effective temperature estimation

The effective temperature (T_{eff1}) of the more massive, and therefore more luminous component (herein defined as the primary star), was derived from a composite (USNO-A2, 2MASS, APASS, Terrell *et al.* 2012) of photometric determinations that were as necessary transformed to (B–V).[1,2] Interstellar extinction (A_V) and reddening ($E(B-V) = A_V/3.1$) was estimated according to a galactic dust map model derived by Schlafly and Finkbeiner (2011). Additional sources used to establish a mean value for each T_{eff1} included the Gaia DR2 release of stellar parameters (Andrae *et al.* 2018), the LAMOST DR6 survey (Zhao *et al.* 2012; Wang *et al.* 2019), and an empirical relationship (Houdashelt *et al.* 2000) based on intrinsic color, $(B-V)_0$. The mean result ($T_{eff1} = 5450 \pm 108$ K) was adopted for WD modeling of LCs from V625 Hya (Table 3).

3.3. LC Modeling with the Wilson-Devinney code

Modeling of LC data (Figure 4) was initially performed with PHOEBE 0.31a (Prša and Zwitter 2005) and then refined using WDwint56a (Nelson 2009). Both programs feature a graphical interface to the Wilson-Devinney WD2003 code (Wilson and Devinney 1971; Wilson 1979, 1990). WDwint56a incorporates Kurucz's atmosphere models (Kurucz 2002) that

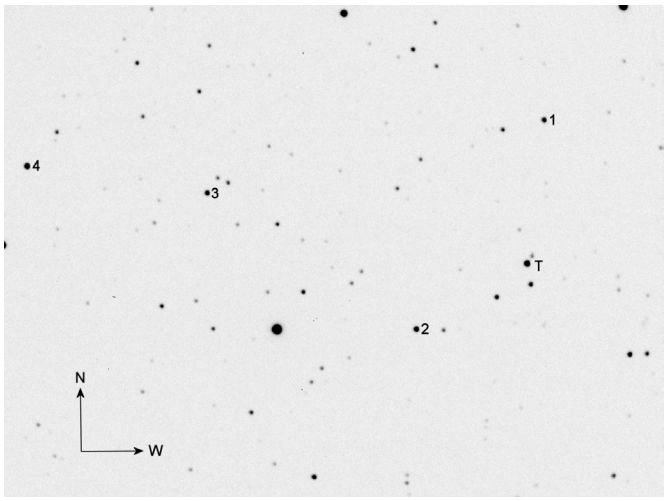

Figure 1. CCD image (V-mag; 90-s) of V625 Hya (T) acquired at DBO (FOV = 15.9 × 21.1 arcmin) showing the location of comparison stars (1–4) used to generate APASS DR9-derived magnitude estimates.

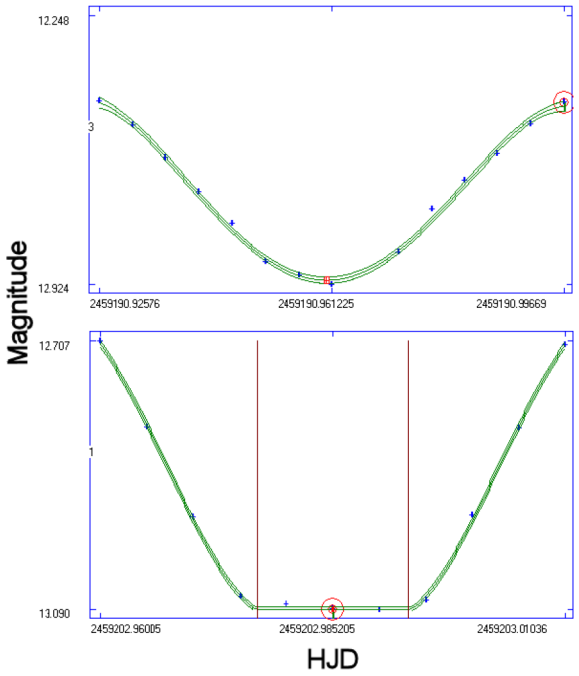

Figure 2. The top panel depicts a representative ToM estimate during Min II using polynomial approximation (α = 4), while the bottom panel shows the fit achieved with the wall-supported line (WSL) algorithm during Min I. In both cases, a red dot signifies the moment of extremum. The boundary lines which indicate the duration of the Min I total eclipse (0.014366 d) are conveniently calculated by MAVKA.

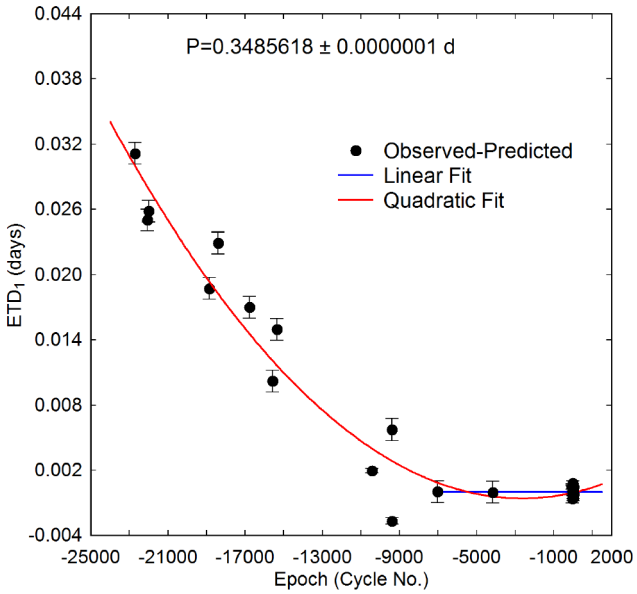

Figure 3. Linear and quadratic fits of ToM differences (ETD_1) vs. epoch for V625 Hya calculated using the new linear ephemeris (Equation 1). Measurement uncertainty is denoted by the error bars.

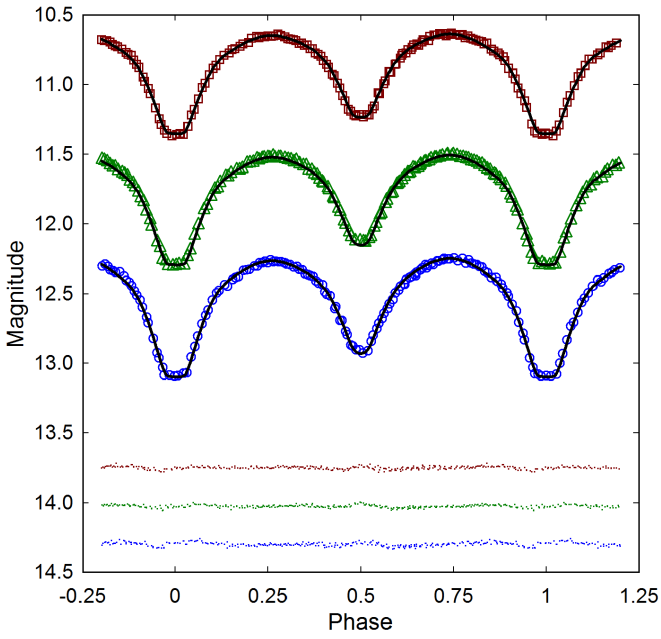

Figure 4. Period-folded (0.3485618 ± 0.0000001 d) CCD-derived LCs for V625 Hya produced from photometric data collected at DBO between 03 December 2020 and 21 December 2020. The top (I_c), middle (V), and bottom curves (B) were transformed to magnitudes based on APASS DR9-derived catalog values from comparison stars. In this case, the model assumed a W-subtype overcontact binary with two cool spots on the primary star; residuals from the model fits are offset at the bottom of the plot to compress the y-axis.

Table 3. Estimation of the primary star effective temperature (T_{eff1}) for V625 Hya.

Parameter	*Value*
DBO $(B–V)_0$[a]	0.727 ± 0.022
Mean combined $(B–V)_0$[a]	0.733 ± 0.018
Galactic reddening E(B–V)[b]	0.0149 ± 0.0004
Survey T_{eff1}[c] (K)	5496 ± 45
Gaia T_{eff1}[d] (K)	5355^{+326}_{-105}
Houdashelt T_{eff1}[e] (K)	5481 ± 282
LAMOST DR5 T_{eff1}[f] (K)	5448 ± 26
Mean T_{eff1} (K)	5450 ± 108
Spectral Class[g]	G7V-G8V

a. Surveys and DBO intrinsic $(B–V)_0$ determined using reddening values (E(B–V)).
b. https://irsa.ipac.caltech.edu/applications/DUST/
c. T_{eff1} interpolated from mean combined $(B–V)_0$ using Table 4 in Pecaut and Mamajek (2013).
d. Values from Gaia DR2 (Gaia Collab. 2016, 2018): http://vizier.u-strasbg.fr/viz-bin/VizieR?-source=I/345/gaia2
e. Values calculated with Houdashelt et al. *(2000) empirical relationship.*
f. Spectral class estimated from LAMOST DR 6 low resolution spectrum = G7V.
g. Spectral class estimated from Pecaut and Mamajek (2013).

Table 4. LC parameters evaluated by WD modeling and the geometric elements derived for V625 Hya (2020) assuming it is a W-type W UMa variable

Parameter[a]	*No Spot*	*Spotted*
T_{eff1} (K)[b]	5450 (108)	5450 (108)
T_{eff2} (K)	5966 (118)	5593 (111)
q (m_2 / m_1)	0.394 (1)	0.431 (1)
A[b]	0.50	0.50
g[b]	0.32	0.32
$\Omega_1 = \Omega_2$	2.624 (2)	2.726 (3)
i°	89.4 (2)	86.1 (3)
$A_P = T_S / T_\star$[c]	—	0.85 (1)
θ_P(spot co-latitude)[c]	—	98.9 (3.2)
φ_P (spot longitude)[c]	—	95.2 (2.8)
r_P (angular radius)[c]	—	10.4 (2)
$A_P = T_S / T_\star$[c]	—	0.77 (1)
θ_P(spot co-latitude)[c]	—	90 (1)
φ_P (spot longitude)[c]	—	180 (1)
r_P (angular radius)[c]	—	18.5 (1)
$L_1 / (L_1 + L_2)_B$[d]	0.5708 (4)	0.6470 (3)
$L_1 / (L_1 + L_2)_V$	0.6054 (3)	0.6565 (2)
$L_1 / (L_1 + L_2)_{I_c}$	0.6322 (3)	0.6641 (2)
r_1 (pole)	0.4421 (4)	0.4292 (4)
r_1 (side)	0.4740 (5)	0.4578 (5)
r_1 (back)	0.5040 (6)	0.4860 (6)
r_2 (pole)	0.2906 (4)	0.2909 (12)
r_2 (side)	0.3042 (5)	0.3037 (14)
r_2 (back)	0.3436 (8)	0.3381 (24)
Fill-out factor (%)	17.6	5.5
RMS (B)[e]	0.01227	0.00944
RMS (V)	0.01035	0.00715
RMS (I_c)	0.01073	0.00763

a. All DBO uncertainty estimates for T_{eff2}, q, $\Omega_{1,2}$, i, $r_{1,2}$, and L_1 from WDWINT56A (Nelson 2009).
b. Fixed with no error during DC.
c. Spot parameters in degrees (θ_P, φ_P and r_P); A_P equals the spot temperature (T_S) divided by star temperature, $T_\star$.
d. L_1 and L_2 refer to scaled luminosities of the primary and secondary stars, respectively.
e. Monochromatic residual mean square error from observed values.

are integrated over BVI_c passbands. The ultimate model selected was Mode 3 for an overcontact binary; other modes (detached and semi-detached) never improved LC simulation as defined by the model residual mean square errors. Since the effective temperature was estimated to be 5450 K, internal energy transfer to the stellar surface is driven by convective (7200 K) rather than by radiative processes (Bradstreet and Steelman 2004). Therefore, bolometric albedo was assigned ($A_{1,2}$ = 0.5) according to Ruciński (1969) while the gravity darkening coefficient was adopted ($g_{1,2}$ = 0.32) from Lucy (1967). Logarithmic limb darkening coefficients (x_1, x_2, y_1, y_2) were interpolated (van Hamme 1993) following any change in the effective temperature during model fit optimization by differential corrections (DC). All but the temperature of the more massive star (T_{eff1}), $A_{1,2}$, and $g_{1,2}$ were allowed to vary during DC iterations. In general, the best fits for T_{eff2}, i, q, and Roche potentials ($\Omega_1 = \Omega_2$) were collectively refined (method of multiple subsets) by DC using the multi-bandpass LC data until a simultaneous solution was found. Most obvious in the B-bandpass, a LC asymmetry (Max I < Max II), the so-called "O'Connell effect" (O'Connell 1951), requires some sort of surface inhomogeneity. Surface inhomogeneity, often associated with star spots, was simulated by the addition of two cool spots on the primary star to obtain the best fit LC models. V625 Hya did not require third light correction (l_3 = 0) to improve WD model fits.

3.4. Wilson-Devinney modeling results

It is generally not possible to unambiguously determine the mass ratio or total mass of an eclipsing binary system without spectroscopic radial velocity (RV) data. In this case the flattened bottom at Min I indicative of a total eclipse suggests that V625 Hya is a W-subtype overcontact binary system (Binnendijk 1970). This finding provided strong motivation to seek a photometric solution for the mass ratio (q_{ptm}) using the WD code. With totality, degeneracy between the radii and inclination is broken (Terrell and Wilson 2005) such that a mass ratio can be determined with very small (< 1%) relative error (Liu 2021).

Standard errors reported in Table 4 are computed from the DC covariance matrix and only reflect the model fit to the observations which assume exact values for any fixed parameter. These formal errors are generally regarded as unrealistically small considering the estimated uncertainties associated with the mean adopted T_{eff1} values along with basic assumptions about $A_{1,2}$, $g_{1,2}$, and the influence of spots added to the WD model. Normally, the value for T_{eff1} is fixed with no error during modeling with the WD code. When T_{eff1} is varied by as much as ± 10%, investigations with other OCBs, including A- (Alton 2019; Alton *et al.* 2020) and W-subtypes (Alton and Nelson 2018), have shown that uncertainty estimates for i, q, or $\Omega_{1,2}$ were not appreciably (< 2.5%) affected. Assuming that the actual T_{eff1} value falls within ± 10% of the adopted values used for WD modeling (a reasonable expectation based on T_{eff1} data provided in Table 4), then uncertainty estimates for i, q, or $\Omega_{1,2}$, along with spot size, temperature, and location, would likely not exceed this amount.

The fill-out parameter (f) which corresponds to the outer surface shared by each star was calculated according to Kallrath and Malone (2009) and Bradstreet (2005) where:

$$f = (\Omega_{inner} - \Omega_{1,2}) / (\Omega_{inner} - \Omega_{outer}) , \quad (3)$$

wherein Ω_{outer} is the outer critical Roche equipotential, Ω_{inner} is the value for the inner critical Roche equipotential, and $\Omega = \Omega_{1,2}$ denotes the common envelope surface potential for the binary system. In this case V625 Hya is considered overcontact since $0 < f < 1$.

There is significant disparity in the mass ratio (0.431 vs. 0.394) and fill-out factor when the LCs are modeled with (5.5%) and without (17.6%) spots. The effects of adding spots to best fit a WD-derived LC model are well documented (Maceroni and van't Veer 1993; Berdyugina 2005; Terrell 2022). A multi-year (1969–2018) study on AU Ser (Alton *et al.* 2018), another OCB, revealed that fill-out factors (4% to 27.3%) were heavily influenced by variously sized spots which were consistently observed in the neck region. Furthermore, during modeling, each spot contributes four additional degrees-of-freedom (size, latitude, longitude, and temperature), challenging attempts to find a global non-degenerate solution. Despite the much smaller residual mean square error from the 2-spot simulation provided herein, the addition of RV data to constrain q and Doppler imaging to map the putative location of spot(s) would be critical to deriving a more robust LC solution for V625 Hya.

Spatial renderings (Figure 5) were produced with Binary Maker 3 (BM3: Bradstreet and Steelman 2004) using the final WDWint56a modeling results from 2020. The smaller secondary is shown to fully transit across the primary face during Min II ($\varphi = 0.5$), thereby confirming that the secondary star is totally eclipsed at Min I.

3.5. Preliminary stellar parameters

Mean physical characteristics were estimated for V625 Hya (Table 5) using results from the best fit (spotted) LC simulations from 2020. Without the benefit of RV data which define the orbital motion, mass ratio, and total mass of the binary pair, these results should be considered "relative" rather than "absolute" parameters and regarded as preliminary. Nonetheless, since the photometric mass ratio (q_{ptm}) is derived from a totally eclipsing OCB, there is a reasonable expectation that DC optimization with the WD2003 code would have arrived at a solution with acceptable uncertainty for q (Terrell and Wilson 2005; Liu 2021).

Calculations are described below for estimating the solar mass and size, semi-major axis, solar luminosity, bolometric V-mag, and surface gravity of each component. Four empirically derived mass-period relationships (M-PR) for W UMa-binaries were used to estimate the primary star mass. The first M-PR was reported by Qian (2003), others followed from Gazeas and Stępień (2008), Gazeas (2009), and more recently Latković *et al.* (2021). According to Qian (2003), when the primary star is less than $1.35\,M_\odot$ or the system is W-type its mass can be determined from:

$$M_1 = 0.391\,(59) + 1.96\,(17) \cdot P, \quad (4)$$

where P is the orbital period in days. This leads to $M_1 = 1.074 \pm 0.084\,M_\odot$ for the primary.

The M-PR derived by Gazeas and Stępień (2008):

Table 5. Fundamental stellar parameters for V625 Hya using the photometric mass ratio ($q_{ptm} = m_2 / m_1$) from the spotted WD model fits of LC data (2020) and the estimated primary star mass based on four empirically derived M-PRs for overcontact binary systems.

Parameter	*Primary*	*Secondary*
Mass ($M_\odot$)	1.146 ± 0.044	0.494 ± 0.019
Radius ($R_\odot$)	1.114 ± 0.011	0.759 ± 0.007
a ($R_\odot$)	2.458 ± 0.024	2.458 ± 0.024
Luminosity ($L_\odot$)	0.987 ± 0.080	0.508 ± 0.041
Mbol	4.765 ± 0.021	5.485 ± 0.088
Log (g)	4.404 ± 0.019	4.371 ± 0.019

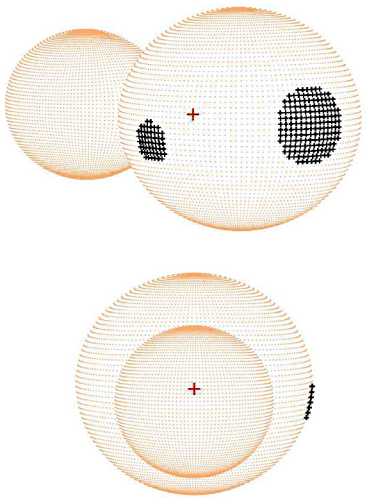

Figure 5. A spatial model of V625 Hya observed during 2020 illustrating (top) the location of two cool (black) spots on the primary star, and (bottom) the secondary star transit across the primary star face at Min II ($\varphi = 0.5$).

$$\log(M_1) = 0.755\,(59) \cdot \log(P) + 0.416\,(24), \quad (5)$$

corresponds to an OCB system where $M_1 = 1.176 \pm 0.098\,M_\odot$.

Gazeas (2009) reported another empirical relationship for the more massive (M_1) star of a contact binary such that:

$$\log(M_1) = 0.725\,(59) \cdot \log(P) - 0.076\,(32) \cdot \log(q) + 0.365\,(32), \quad (6)$$

from which $M_1 = 1.151 \pm 0.050\,M_\odot$.

Finally, Latković *et al.* (2021) conducted an exhaustive analysis from nearly 700 W UMa stars in which they established mass-period, radius-period, and luminosity-period relationships for the primary and secondary stars. Accordingly, the M-PR:

$$M_1 = (2.94 \pm 0.21 \cdot P) + (0.16 \pm 0.08), \quad (7)$$

leads to a primary star mass of $1.185 \pm 0.108\,M_\odot$.

The mean from these four values ($M_1 = 1.146 \pm 0.044\,M_\odot$) was used for subsequent determinations of M_2, semi-major axis a, volume-radii r_L, and bolometric magnitudes (M_{bol}) using the formal errors calculated by WDWint56a (Nelson 2009).

The secondary mass ($0.494 \pm 0.019\,M_\odot$) and total mass ($1.640 \pm 0.048\,M_\odot$) were determined using the photometric mass ratio ($q_{ptm} = 0.431 \pm 0.001$) derived from the best fit (spotted) model.

The semi-major axis, $a(R_\odot) = 2.458 \pm 0.024$, was calculated from Newton's version of Kepler's third law where:

$$a^3 = G \cdot P^2 (M_1 + M_2) / 4\pi^2. \quad (8)$$

The effective radius of each Roche lobe (r_L) can be calculated over the entire range of mass ratios ($0 < q < \infty$) according to an expression derived by Eggleton (1983):

$$r_L = 0.49q^{(2/3)} / (0.6q^{(2/3)} + \ln(1 + q^{(1/3)})), \quad (9)$$

from which values for r_1 (0.4533 ± 0.0003) and r_2 (0.3089 ± 0.0002) were determined for the primary and secondary stars, respectively. The radii in solar units for both binary components can be calculated such that $R_1 = a \cdot r_1 = 1.114 \pm 0.011\ R_\odot$ and $R_2 = a \cdot r_2 = 0.759 \pm 0.007\ R_\odot$.

Luminosity in solar units ($L_\odot$) for the primary (L_1) and secondary stars (L_2) was calculated from the well-known relationship derived from the Stefan-Boltzmann law where:

$$L_{1,2} = (R_{1,2} / R_\odot)^2 (T_{1,2} / T_\odot)^4. \quad (10)$$

Assuming that $T_{eff1} = 5450$ K, $T_{eff2} = 5593$ K, and $T_\odot = 5772$ K, then the solar luminosities ($L_\odot$) for the primary and secondary are $L_1 = 0.987 \pm 0.080$ and $L_2 = 0.508 \pm 0.041$, respectively.

4. Conclusions

The results from this first detailed investigation of V625 Hya have supplemented an increasingly expanding list of W UMa-type variables that have been physically and geometrically characterized using a reliable mass ratio. Similar to other W-type OCBs, V625 Hya is comprised of relatively cool (late spectral class G) stars orbiting their common gravitational center in less than 0.4~d. In addition, all LCs exhibited a flattened bottom during Min I, a characteristic feature typically observed with totally eclipsing W-subtype systems. Sixteen new ToM values were determined from LCs acquired at DBO in 2020. These, along with eleven other values extrapolated from four surveys (1999–2016) employing sparse-sampling strategies and two from the literature, led to updated linear and quadratic ephemerides. Secular analyses suggested that the orbital period of V625 Hya is changing at a rate ($+0.0137\ s \cdot y^{-1}$) consistent with other similarly classified OCBs. The photometric mass ratio ($q_{ptm} = 0.417 \pm 0.003$) determined by WD modeling is expected to compare favorably with a mass ratio (q_{sp}) derived from RV data. Regardless, spectroscopic studies (RV and high resolution classification spectra) are necessary to unequivocally determine a total mass and spectral class for this binary system. Consequently, all parameter values and corresponding uncertainties reported herein should be considered preliminary.

5. Acknowledgements

This research has made use of the SIMBAD database operated at Centre de Données astronomiques de Strasbourg, France. In addition, the Northern Sky Variability Survey hosted by the Los Alamos National Laboratory (https://skydot.lanl.gov/nsvs/nsvs.php), the All-Sky Automated Survey (http://www.astrouw.edu.pl/asas/? page=acvs), the All-Sky Automated Survey for Supernovae (https://asas-sn.osu.edu/variables), the Catalina Sky Survey (http://nesssi.cacr.caltech.edu/DataRelease/), and the International Variable Star Index (AAVSO) were mined for essential information. This work also presents results from the European Space Agency (ESA) space mission Gaia. Gaia data are being processed by the Gaia Data Processing and Analysis Consortium (DPAC). Funding for the DPAC is provided by national institutions, in particular the institutions participating in the Gaia MultiLateral Agreement (MLA). The Gaia mission website is https://www.cosmos.esa.int/gaia. The Gaia archive website is https://archives.esac.esa.int/gaia. This paper makes use of data from the first public release of the WASP data as provided by the WASP consortium and services at the NASA Exoplanet Archive, which is operated by the California Institute of Technology, under contract with the National Aeronautics and Space Administration under the Exoplanet Exploration Program. The use of public data from LAMOST (http://dr6.lamost.org/) is also acknowledged. Guoshoujing Telescope (the Large Sky Area Multi-Object Fiber Spectroscopic Telescope LAMOST) is a National Major Scientific Project built by the Chinese Academy of Sciences. Funding for the project has been provided by the National Development and Reform Commission. LAMOST is operated and managed by the National Astronomical Observatories, Chinese Academy of Sciences. Many thanks to the anonymous referee and Editor Morrison, both of whom provided valuable commentary along with corrections.

References

Akerlof, C., *et al.* 2000, *Astron. J.*, **119**, 1901.

Alton, K. B. 2019, *J. Amer. Assoc. Var. Star Obs.*, **47**, 7.

Alton, K. B., and Nelson, R. H. 2018, *Mon. Not. Roy. Astron. Soc.*, **479**, 3197.

Alton, K. B., Nelson, R. H. and Stępień, K. 2020, *J. Astrophys. Astron.*, **41**, 26.

Alton, K. B., Nelson, R. H., and Terrell, D. 2018, *Info. Bull. Var. Stars*, No. 6256, 1.

Andrae, R., *et al.* 2018, *Astron. Astrophys.*, **616A**, 8.

Andrych, K. D. and Andronov, I. L. 2019, *Open Eur. J. Var. Stars*, **197**, 65.

Andrych, K. D., Andronov, I. L., and Chinarova, L. L. 2017, *Odessa Astron. Publ.*, **30**, 57.

Andrych, K. D., Andronov, I. L., and Chinarova, L. L. 2020, *J. Phys. Stud.*, **24**, 1902.

Berdyugina, S. V. 2005, *Living Rev. Solar Phys.*, **2**, 8.

Berry, R., and Burnell, J. 2005, *The Handbook of Astronomical Image Processing*, 2nd ed., Willmann-Bell, Richmond, VA.

Binnendijk, L. 1970, *Vistas Astron.*, **12**, 217.

Bradstreet, D. H. 2005, in *The Society for Astronomical Sciences 24th Annual Symposium on Telescope Science*, Society for Astronomical Sciences, Rancho Cucamonga, CA, 23.

Bradstreet, D. H., and Steelman, D. P. 2004, Binary Maker 3, Contact Software (http://www.binarymaker.com).

Diethelm, R. 2011, *Info. Bull. Var. Stars*, No. 5992, 1.

Diethelm, R. 2012, *Info. Bull. Var. Stars*, No. 6011, 1.
Drake, A. J., *et al.* 2014, *Astrophys. J., Suppl. Ser.*, **213**, 9.
Eggleton, P. P. 1983, *Astrophys. J.*, **268**, 368.
Gaia Collaboration, *et al.* 2016, *Astron. Astrophys.*, **595A**, 1.
Gaia Collaboration, *et al.* 2018, *Astron. Astrophys.*, **616A**, 1.
Gazeas, K. D. 2009, *Commun. Asteroseismology*, **159**, 129.
Gazeas, K., and Stępień, K. 2008, *Mon. Not. Roy. Astron. Soc.*, **390**, 1577.
Gettel, S. J., Geske, M. T., and McKay, T. A. 2006, *Astron. J.*, **131**, 621.
Henden, A. A., Levine, S. E., Terrell, D., Smith, T. C., and Welch, D. L. 2011, *Bull. Amer. Astron. Soc.*, **43**, 2011.
Henden, A. A., Terrell, D., Welch, D., and Smith, T. C. 2010, *Bull. Amer. Astron. Soc.*, **42**, 515
Henden, A. A., Welch, D. L., Terrell, D., and Levine, S. E. 2009, *Bull. Amer. Astron. Soc.*, **41**, 669.
Hoffman, D. I., Harrison, T. E., and McNamara, B. J. 2009, *Astron. J.*, **138**, 466.
Houdashelt, M. L., Bell, R. A., and Sweigart, A. V. 2000, *Astron. J.*, **119**, 1448.
Howell, S. B. 2006, *Handbook of CCD Astronomy*, 2nd ed., Cambridge Univ. Press., Cambridge.
IONDEV SRL. 2021, QtiPlot—Data Analysis and Scientific Visualisation (https://www.qtiplot.com/).
Jayasinghe, T., *et al.* 2018, *Mon. Not. Roy. Astron. Soc.*, **477**, 3145.
Kafka, S. 2021, *Observations from the AAVSO International Database* (https://www.aavso.org/data-download).
Kallrath, J., and Milone, E. F. 2009, *Eclipsing Binary Stars: Modeling and Analysis*, Springer-Verlag, New York.
Kurucz, R. L. 2002, *Baltic Astron.*, **11**, 101.
Latković, O., Čeki, A., and Lazarević, S. 2021, *Astrophys. J., Suppl. Ser.*, **254**, 10.
Li, K., *et al.* 2019, *Res. Astron. Astrophys.*, **19**, 147.
Liu, L. 2021, *Publ. Astron. Soc. Pacific*, **133**, 084202.
Lucy, L. B. 1967, *Z. Astrophys.*, **65**, 89.
Maceroni, C., and van't Veer, F. 1993, *Astron. Astrophys.*, **277**, 515.
Minor Planet Observer. 2011, MPO Canopus v 10.7.1.3 (http://www.minorplanetobserver.com).
Mortara, L., and Fowler, A. 1981, in *Solid State Imagers for Astronomy*, SPIE Conf. Proc. 290, Society for Photo-Optical Instrumentation Engineers, Bellingham, WA, 28.
Nelson, R. H. 2009, WDwint56a: Astronomy Software by Bob Nelson (https://www.variablestarssouth.org/bob-nelson).
O'Connell, D. J. K. 1951, *Publ. Riverview Coll. Obs.*, **2**, 85.
Pecaut, M. J., and Mamajek, E. E. 2013, *Astrophys. J., Suppl. Ser.*, **208**, 9.
Pojmański, G., Pilecki, B., and Szczygiel, D. 2005, *Acta Astron.*, **55**, 275.
Prša, A., and Zwitter, T. 2005, *Astrophys. J.*, **628**, 426.
Qian, S. 2001, *Mon. Not. Roy. Astron. Soc.*, **328**, 635.
Qian, S. 2003, *Mon. Not. Roy. Astron. Soc.*, **342**, 1260.
Ruciński, S. M. 1969, *Acta Astron.*, **19**, 245.
Schlafly, E. F., and Finkbeiner, D. P. 2011, *Astrophys. J.*, **737**, 103.
Shappee, B. J., *et al.* 2014, *Astrophys. J.*, **788**, 48.
Smith, T. C., Henden, A. A., and Starkey, D. R. 2011, in *The Society for Astronomical Sciences 30th Annual Symposium on Telescope Science*, Society for Astronomical Sciences, Rancho Cucamonga, CA, 121.
Software Bisque. 2019, The Sky X professional edition 10.5.0 (https://www.bisque.com).
Terrell, D. 2022, *Galaxies*, **10**, 8.
Terrell, D., and Wilson, R. E. 2005, *Astrophys. Space Sci.*, **296**, 221.
Terrell, D., Gross, J., and Cooney, W. R. 2012, *Astron. J.*, **143**, 99.
van Hamme, W. 1993, *Astron. J.*, **106**, 2096.
Wang, R., *et al.* 2019, *Publ. Astron. Soc. Pacific*, **131**, 024505.
Wilson, R. E. 1979, *Astrophys. J.*, **234**, 1054.
Wilson, R. E. 1990, *Astrophys. J.*, **356**, 613.
Wilson, R. E., and Devinney, E. J. 1971, *Astrophys. J.*, **166**, 605.
Woźniak, P. R., *et al.* 2004, *Astron. J.*, **127**, 2436.
Zhao, G., Zhao, Y.-H., Chu, Y.-Q., Jing, Y.-P., and Deng, L.-C. 2012, *Res. Astron. Astrophys.*, **12**, 723.